

Deep learning to discover and predict dynamics on an inertial manifold

Alec J. Linot¹ and Michael D. Graham^{1,*}

¹*Department of Chemical and Biological Engineering,
University of Wisconsin-Madison, Madison WI 53706, USA*

(Dated: March 13, 2022)

A data-driven framework is developed to represent chaotic dynamics on an inertial manifold (IM), and applied to solutions of the Kuramoto-Sivashinsky equation. A hybrid method combining linear and nonlinear (neural-network) dimension reduction transforms between coordinates in the full state space and on the IM. Additional neural networks predict time-evolution on the IM. The formalism accounts for translation invariance and energy conservation, and substantially outperforms linear dimension reduction, reproducing very well key dynamic and statistical features of the attractor.

Partial differential equations such as the Navier-Stokes equations that govern fluid motion are formally infinite-dimensional, but the presence of dissipation (through viscosity or diffusion, for example) leads to the expectation that the long-time dynamics collapse onto a finite-dimensional invariant manifold, as noted by Hopf [1]. Specifically, for some systems, including the Kuramoto-Sivashinsky equation (KSE) that we consider here, it can be proven that all initial conditions exponentially approach an *inertial manifold* \mathcal{M} of finite dimension $d_{\mathcal{M}}$ [2], on which the long time dynamics evolve. For $u \in \mathcal{M}$, one can find a coordinate transformation $h = \chi(u)$ to coordinates h on the inertial manifold, a change of coordinates $u = \tilde{\chi}(h)$ back to the full space, and a dynamical system $h(t + \tau) = F(h(t))$ on \mathcal{M} . (Alternately, one could represent the dynamical system in differential form $dh/dt = G(h)$.) This dynamical system is an exact reduced-order model (ROM). Such a model can be practically useful, for computationally efficient simulations of a complex process, and may also be fundamentally important, since the coordinates h represent the key dynamical variables for the phenomenon of interest.

In the present work, we use “data” in the form of chaotic solutions to the KSE with periodic boundary conditions, to find neural-network (NN) representations of the functions χ , $\tilde{\chi}$, and F . Many prior studies of inertial manifolds, and approximations thereof, take the inertial manifold to be the graph of a function Φ such that $\mathcal{M} := \{u_+ + \Phi(u_+)\}$, where $u_+ = P_N u$ is a linear projection onto, for example, a small number of eigenfunctions of the Laplacian [3–5]. The present work is not subject to such assumptions. Our formalism explicitly accounts for the important physical features of translation invariance and energy conservation found in this system (and others, such as the Navier-Stokes equations), and reproduces very well, with a minimal number of degrees of freedom, key dynamic and statistical features of the attractor.

A standard machine learning method for nonlinear dimension reduction is the undercomplete autoencoder [6, 7]. This is a pair of neural networks, one mapping from a high-dimensional space to a low-dimensional one, and the second doing the reverse. The networks take data u as input, compute an output \tilde{u} and are trained to minimize a loss function $L = \|u - \tilde{u}\|^2$ summed over a batch of data vectors u . Autoencoders have been used for nonlinear dimension reduction in many applications [6], including turbulent flow fields [8]. For dynamical systems, autoencoders have been used to explicitly yield coordinate transformations on which the dynamics are linear [9, 10] (e.g. to determine eigenmodes of the Koopman operator) or have a sparse representation [11]. Gonzalez et al. [12] have combined autoencoders with nonlinear time-evolution models for reconstruction of dynamics of isotropic turbulence and lid-driven cavity flow. Lee and Carlberg [13] give an overview of nonlinear model reduction with NNs and application to transient dynamics of Burgers equation.

Other studies have focused on developing NNs for evolving equations with chaotic dynamics without nonlinear dimension reduction. In [14] proper orthogonal decomposition (POD) and a spectral version (SPOD), both linear dimension reduction techniques, were used to reduce the dimension of fluid flow data that were then used to train a NN for time evolution. Vlachas et al. [15] combined various linear dimension reduction approaches with a long-short term memory NN and mean stochastic modeling to keep trajectories on the attractor. Pathak et al. [16] showed reservoir learning to be a highly effective method of predicting dynamics of the KSE. Finally, in [17], an autoencoder is used to estimate $d_{\mathcal{M}}$ for the dynamics of the complex Ginzburg-Landau equation; however the dynamics on \mathcal{M} are not modeled. The present work combines dimension reduction and time evolution using an efficient autoencoder structure and incorporation of translation symmetry and

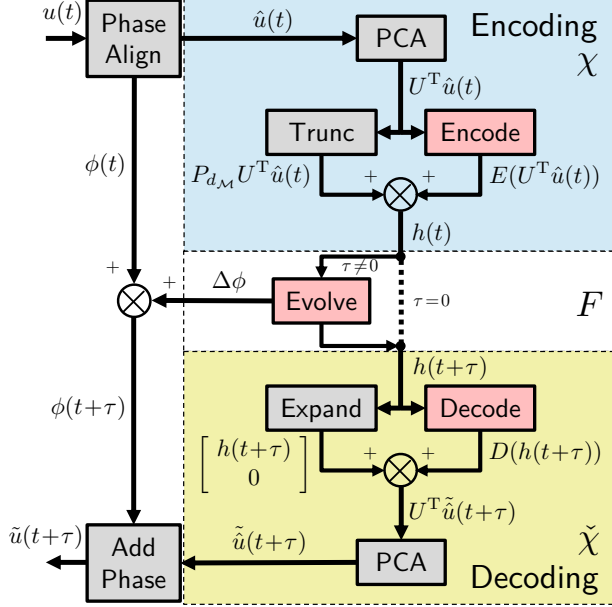


FIG. 1: Block diagram for the hybrid autoencoder and time-evolution scheme. NNs are pink.

energy conservation.

The testbed for this approach is the KSE,

$$\partial_t u = -u \partial_x u - \partial_{xx} u - \partial_{xxxx} u, \quad (1)$$

with periodic boundary conditions in the domain $x \in [0, L]$. We select $L = 22$ because it yields chaotic dynamics that have been well studied [18]. Solutions to this equation are only unique to within a translation that we will represent with a phase variable ϕ . This equation has an energy conservation principle: when time-averaged, the energy production rate $\mathcal{P} = \langle \partial_x u \partial_x u \rangle$ balances the dissipation rate $\varepsilon = \langle \partial_{xx} u \partial_{xx} u \rangle$. Here $\langle \cdot \rangle$ represents averaging over x . These properties are incorporated into the dimension reduction formulation as detailed below. Trajectories were generated using a Fourier spectral method in space and a fourth-order time integration scheme [19] with the code available from Cvitanović et al. [20]. The solution u is represented on a uniformly spaced mesh of 64 points, so the dimension d of the full state space is $d = 64$.

Figure 1 illustrates our framework for finding the inertial manifold and the dynamical system on it. The first step of the process exploits translation invariance: the solution u at every time instant is transformed into a pattern \hat{u} and a phase ϕ using an approach called the “method of slices” [21, 22]. We take the discrete Fourier transform \mathcal{F} of our data in x to yield $a(t) = \mathcal{F}\{u(t)\}$. With the data in Fourier space, the phase of the first Fourier mode $a_1(t)$ is found using $\phi(t) = \text{atan2}(\text{Im}(a_1(t)), \text{Re}(a_1(t)))$.

TABLE I: Architectures of the NNs. “Shape” indicates the dimension of each layer, and “activation” the corresponding activation functions (S is the sigmoid activation)[7].

	Function	Shape	Activation
Encoder	E	$d : 500 : d_h$	S: tanh
Decoder	D	$d_h : 500 : d$	S: linear
Evolution	F_h	$d_h : 200 : 200 : d_h$	S: S: linear
Evolution	F_ϕ	$d_h : 500 : 50 : 500 : 1$	S: S: S: linear

Now we can construct a phase-aligned solution $\hat{u}(t)$ so that its first Fourier mode is a pure cosine : $\hat{u}(t) = \mathcal{F}^{-1}\{a(t)e^{-ik\phi(t)}\}$. Storage of ϕ for each data vector allows conversion of \hat{u} back to u . Times when $a_1(t)$ approaches zero require special treatment, as was recognized by Budanur et al. [21]. We use the solution they proposed, which is to stretch time according to $\Delta \hat{t} = \Delta t / |a_1(t)|$. The rescaled time \hat{t} is called “in-slice” time. There is no barrier to moving back and forth between real time and in-slice time because the transformation is given implicitly by the solutions at a given time $u(t)$. The data used for training the NNs were $4 \cdot 10^6$ solutions u separated by $\Delta \hat{t} = 0.2$ “in-slice” time units, which corresponds to $\Delta t \approx 0.023$ time units on average. Data was gathered after the dynamics had settled onto the attractor.

Given the phase-aligned pattern data \hat{u} , the first machine learning task is to find the manifold \mathcal{M} , of dimension $d_{\mathcal{M}}$ on which this data lives, or equivalently the coordinate transformations $h = \chi(\hat{u})$ and $\hat{u} = \tilde{\chi}(h)$. Because the phase of any given data vector u is arbitrary, the phase information is not needed for this step. (For a discussion of invariant manifolds in translation-symmetric systems, see Ref. [22].) Indeed, phase alignment allows more efficient representation of the data, because phase information need not be encoded – it is captured separately as noted above.

To find χ and $\tilde{\chi}$, we use a variant of a standard undercomplete autoencoder, shown for $\tau = 0$ in Figure 1. This variant uses a NN to represent the *difference* between the data and its projection onto the basis arising from principal components analysis (PCA) of the data set [23]. PCA is widely used for linear dimension reduction because it yields the projection of dimension d_h that minimizes the mean squared deviation from the original data. Let U be a square orthogonal matrix whose columns are the PCA basis vectors, and $P_{d_h} U^T$ and $P_{d-d_h} U^T$ the projection onto the first d_h and last $d - d_h$ such vectors, respectively. The encoding step learns the function

$E(U^T \hat{u}(t))$ such that

$$E(U^T \hat{u}(t)) = h(t) - P_{d_h} U^T \hat{u}(t). \quad (2)$$

This structure is shown inside the blue box in Figure 1. It must be emphasized that there is no approximation in choosing this representation. Furthermore, U need not come from PCA – any other set of basis vectors, Fourier modes for example, could also be used.

The decoding step takes the data $h(t)$ in the inertial manifold coordinates and transforms it back to the full space, as shown in the yellow box in Figure 1. Again one can think of learning a difference: the decoder learns a function $D(h(t))$ such that

$$D(h(t)) = U^T \tilde{u}(t) - \begin{bmatrix} h(t) \\ 0 \end{bmatrix}. \quad (3)$$

Taking $E(U^T \hat{u}(t)) = 0$ recovers the original IM formulation, but precludes the representation of curved manifolds that do not have a one-to-one mapping to a linear projection. An example of such a manifold is the Archimedean spiral, whose Cartesian representation is $(x, y) = (\phi \cos \phi, \phi \sin \phi)$. The autoencoder architecture used here is able to represent this manifold with $d_h = 1$.

Finally, inserting Eq. 2 into Eq. 3, solving for \tilde{u}_t , and noting that this can be written $\tilde{u}(t) = U [P_{d_h} U^T \hat{u}(t), P_{d-d_h} U^T \hat{u}(t)]^T$, shows that the exact solution satisfies $E(U^T \hat{u}(t)) + D_{d_h}(h(t)) = 0$, where D_{d_h} contains the first d_h components of D . This constraint can be satisfied approximately by adding a penalty term to the autoencoder loss function so it becomes

$$L = \|\hat{u}(t) - \tilde{u}(t)\|^2 + \alpha \|E(\hat{u}(t)) + D_{d_h}(h(t))\|^2. \quad (4)$$

With this structure, we can in principle achieve an exact representation (within the approximation error of the functions E and D) of data on a manifold of dimension d_M for all $d_h \geq d_M$.

Autoencoders of the above structure were trained using the phase aligned data. For comparison, we also trained two standard autoencoders with loss $L = \|\hat{u} - \tilde{u}\|^2$, one without the PCA coordinate transformations and the other with it. All NN used the same architecture for D and E . The architectures for these NNs appear in Table I. Twenty HNNs, with $\alpha = 1$, and standard autoencoders were trained at a given d_h for 1000 epochs with an Adam optimizer using Keras [24]. This process was repeated for a range of d_h . Results are reported for the best model at each value of d_h .

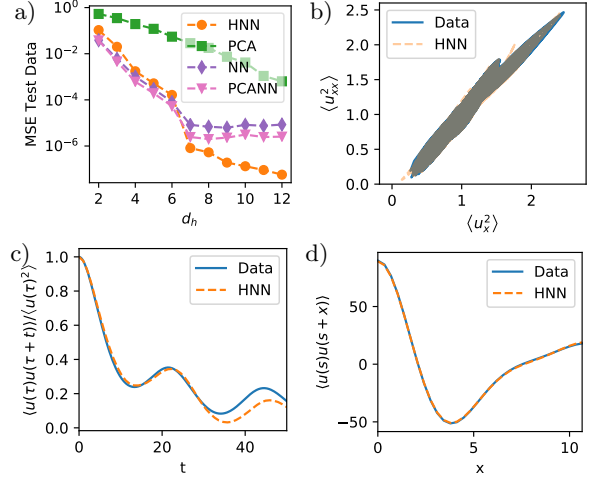


FIG. 2: (a) MSE of test data for various d_h . (b) \mathcal{P} vs. ε state-space projection for the data and HNN ROM prediction. (c) time-correlation function for the data and HNN ROM prediction with $d_h = 7$. (d) spatial correlation function for the data and HNN ROM prediction with $d_h = 7$.

Figure 2a shows the mean squared error (MSE) on a separate test dataset for the NN methods and for PCA. At low d_h , the HNN and standard NNs perform similarly, and in both cases the MSE drops significantly at $d_h = 7$. All NNs perform orders of magnitude better than PCA. On continuing to increase d_h , the HNN continues to improve, while the standard NNs, with a change of basis (PCANN) and without (NN), stagnate. Notably, the abrupt drop in MSE at $d_h = 7$ coincides with the true dimension d_M of the attractor, as found in [25]. The remaining error for $d_h \geq 7$ for the HNN is small, at $O(10^{-7})$, which follows from the fact that at this dimension an exact coordinate transformation exists, so the remaining error is approximation error.

Having in hand the coordinate representation for points on \mathcal{M} , we now use NNs to learn the dynamical system on the manifold, corresponding to $\tau \neq 0$ in Figure 1. We construct discrete time mappings

$$h(t+\tau) = F_h(h(t)), \quad \Delta\phi \equiv \phi(t+\tau) - \phi(t) = F_\phi(h(t)), \quad (5)$$

where F_h and F_ϕ have the architectures shown in Table I. We set $\tau = 2$ “in-slice” time units.

Recall that the energy balance for the KSE requires that the production and dissipation rates \mathcal{P} and ε must balance on average. We incorporate this fact in the training of the dynamic models as follows. We compute the projection of the data onto \mathcal{P} and ε , as shown in Figure 2b. This is narrowly distributed around the line $\mathcal{P} = \varepsilon$ with a sharp boundary, and we can find maximum and minimum dissipation rates

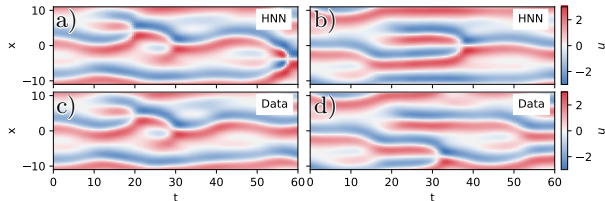


FIG. 3: (a) and (b) two trajectories generated with the HNN ROM. (c) and (d) true trajectories corresponding to (a) and (b).

ε_{\max} and ε_{\min} associated with a given value of \mathcal{P} . We then add a penalty to the loss function L_F for F_h and F_ϕ for crossing this boundary, yielding

$$L_F = \|u(t + \tau) - \tilde{u}(t + \tau)\|^2 + \beta \max(\max(0, \tilde{\varepsilon} - \varepsilon_{\max}(\tilde{\mathcal{P}})), \varepsilon_{\min}(\tilde{\mathcal{P}}) - \tilde{\varepsilon}), \quad (6)$$

where $\tilde{\mathcal{P}}$ and $\tilde{\varepsilon}$ are calculated from \tilde{u} . We selected $\beta = 0.1$ so the second term contributed the same order of error to the loss as the first term. For each d_h , the best dimension reduction model was chosen, and fifty time-evolution models were trained for 200 epochs. Results are reported for the best models.

For a given initial condition $u(0)$ on the manifold, we can find initial conditions $h(0)$ and $\phi(0)$ from the phase-alignment and coordinate transformation (encoding) steps, and then step forward in time with Eq. 5. (At any given time, $u(t)$ can be reconstructed from $\tilde{\chi}(h(t))$ and $\phi(t)$.) Figures 3a and 3b show the evolution of two initial conditions of test data using the dynamical system found with $d_h = d_{\mathcal{M}} = 7$, as well as the “exact” results (3c and 3d) obtained from solving the KSE. In both cases, the model results, which we denote HNN ROM, closely track the exact evolution for 30 or more time units before diverging. This is very good performance for predictions of chaotic dynamics; the integral time for this data is $1.9 \cdot 10^1$ and the Lyapunov time is $2.1 \cdot 10^1$ [25]. The time-correlation function for the data and HNN ROM prediction is shown in Figure 2c – these are in good agreement for $t \lesssim 30$, and the spatial auto-correlation function is shown in Figure 2d – here very close agreement is found. Figure 2b shows that the HNN ROM prediction stays within the envelope of the energy balance, which was the intent of the penalty in the loss.

To further evaluate the performance of this modeling framework, we now describe how the model predictions vary with d_h and compare to predictions from linear dimension reduction with PCA and NNs for the dynamics, denoted PCA ROM. For these comparisons, we present the joint probability density function (PDF) of the pointwise values of u_x and

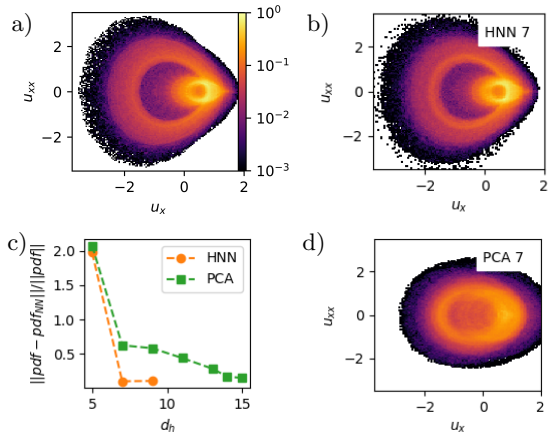


FIG. 4: (a) joint PDF of data. (b) joint PDF of HNN ROM prediction. (c) Relative error in PDF vs dimension. (d) joint PDF of PCA ROM prediction.

u_{xx} , because of their relevance for the overall energy balance. Figure 4a shows this PDF, on a log scale, as determined from the data. At $d_h = d_{\mathcal{M}} = 7$, the HNN ROM prediction, Figure 4b, is very close to the exact PDF. At the same dimension, Figure 4d shows the PCA ROM prediction yields much poorer results. Figure 4c shows how the relative L_2 difference between the true PDF and the model predictions varies with d_h . For $d_h = 5$, the predictions are poor for both cases, but for $d_h \geq 7$, the error is small and nearly unchanging for the HNN ROM case, which is unsurprising since $d_{\mathcal{M}} = 7$. On the other hand, it takes $d_h = 14$ for the PCA ROM to yield a comparable model to the HNN ROM at $d_h = 7$. This result might be expected based on Whitney’s embedding theorem, which states that any manifold of dimension k can be embedded in \mathbb{R}^{2k} [26].

We have shown here a framework for data-driven “exact” reduction of a dynamical system onto a low dimensional invariant manifold and time-evolution on that manifold. Translation symmetry and energy conservation, two important features of many systems of interest, are incorporated naturally into the framework. By observing the model reduction error as a function of dimension, the dimension $d_{\mathcal{M}}$ of the invariant manifold can be determined, and once $d_{\mathcal{M}}$ is known, highly accurate model predictions can be obtained. In particular, key statistical quantities in a chaotic system can be well-approximated, indicating that the model dynamics capture the shape of the attractor. Extensions to systems with higher-dimensional dynamics are underway. Systematizing this method could provide an easily interpretable, data-driven means of approximating the dimension of manifolds, a difficult task for high-dimensional chaotic systems like turbulence.

This work was supported by AFOSR FA9550-18-1-0174 and ONR N00014-18-1-2865.

* mdgraham@wisc.edu

- [1] E. Hopf, *Communications on Pure and Applied Mathematics* **1**, 303 (1948).
- [2] C. Foias, B. Nicolaenko, G. R. Sell, and R. Temam, *J. Math. Pure Appl.* **67**, 197 (1988).
- [3] S. Zelik, *Proceedings of the Royal Society of Edinburgh Section A: Mathematics* **144**, 1245 (2013), [arXiv:1303.4457](https://arxiv.org/abs/1303.4457).
- [4] C. Foias, G. R. Sell, and R. Temam, *Journal of Differential Equations* **73**, 309 (1988).
- [5] M. D. Graham, P. H. Steen, and E. S. Titi, *J Non-linear Sci* **3**, 153 (1993).
- [6] G. E. Hinton and R. R. Salakhutdinov, *Science* **313**, 504 (2006).
- [7] I. Goodfellow, Y. Bengio, and A. Courville, *Deep Learning* (MIT Press, 2016) <http://www.deeplearningbook.org>.
- [8] N. Omata and S. Shirayama, *AIP Advances* **9**, 015006 (2019).
- [9] S. E. Otto and C. W. Rowley, *SIAM Journal on Applied Dynamical Systems* **18**, 558 (2019).
- [10] B. Lusch, J. N. Kutz, and S. L. Brunton, *Nat Comms* **9**, 851 (2018).
- [11] K. Champion, B. Lusch, J. N. Kutz, and S. L. Brunton, *ArXiv* (2019), [1904.02107v2](https://arxiv.org/abs/1904.02107v2).
- [12] F. J. Gonzalez and M. Balajewicz, *ArXiv* (2018), [1808.01346v2](https://arxiv.org/abs/1808.01346v2).
- [13] K. Lee and K. T. Carlberg, *Journal of Computational Physics* , 108973 (2019).
- [14] H. F. Lui and W. R. Wolf, *Journal of Fluid Mechanics* **872**, 963 (2019).
- [15] P. R. Vlachas, W. Byeon, Z. Y. Wan, T. P. Sapsis, and P. Koumoutsakos, *Proceedings of the Royal Society A: Mathematical, Physical and Engineering Sciences* **474**, 20170844 (2018).
- [16] J. Pathak, B. Hunt, M. Girvan, Z. Lu, and E. Ott, *Phys. Rev. Lett.* **120**, 024102 (2018).
- [17] P. V. Kuptsov and A. V. Kuptsova, in *Saratov Fall Meeting 2018: Computations and Data Analysis: from Nanoscale Tools to Brain Functions*, edited by D. E. Postnov (SPIE, 2019).
- [18] P. Cvitanović, R. L. Davidchack, and E. Siminos, *SIAM Journal on Applied Dynamical Systems* **9**, 1 (2010), [arXiv:0709.2944](https://arxiv.org/abs/0709.2944).
- [19] A.-K. Kassam and L. N. Trefethen, *SIAM Journal on Scientific Computing* **26**, 1214 (2005).
- [20] P. Cvitanović, R. Artuso, R. Mainieri, G. Tanner, and G. Vattay, *Chaos: Classical and Quantum* (Niels Bohr Inst., Copenhagen, 2016).
- [21] N. B. Budanur, D. Borrero-Echeverry, and P. Cvitanović, *Chaos* **25**, [10.1063/1.4923742](https://doi.org/10.1063/1.4923742) (2015).
- [22] N. B. Budanur, P. Cvitanović, R. L. Davidchack, and E. Siminos, *Physical Review Letters* **114**, 1 (2015).
- [23] G. Strang, *Linear algebra and learning from data* (Wellesley-Cambridge Press, 2019).
- [24] F. Chollet *et al.*, Keras, <https://keras.io> (2015).
- [25] X. Ding, H. Chaté, P. Cvitanović, E. Siminos, and K. A. Takeuchi, *Physical Review Letters* **117**, 1 (2016).
- [26] V. Guillemin and A. Pollack, *Differential Topology* (AMS Chelsea Publishing, Providence, Rhode Island, 2000).